Ionoluminescence properties of polystyrene-hosted fluorophore films induced by helium ions of energy 50–350 keV

Subha Chakraborty and Mengbing Huang[*]

The College of Nanoscale Science and Engineering (CNSE), SUNY Polytechnic Institute, Albany, New York 12203, USA
(Received 26 April 2017; published 4 October 2017)

We report on measurements and analysis of ionoluminescence properties of pure polystyrene films and polystyrene films doped with four types of fluorophores in low kinetic energies (50–350 keV) of ion irradiation. We have developed a theoretical model to understand the experimentally observed ionoluminescence behaviors in terms of scintillation yield from individual ion tracks, photophysical energy transfer mechanisms, and irradiation-induced defects. A comparison of the model and experimental results suggests that singlet up-conversion resulting from triplet-triplet annihilation processes may be responsible for enhanced singlet emission of the fluorophores at high ion beam flux densities. Energy transfer from the polystyrene matrix to the fluorophore molecules has been identified as an effective pathway to increasing the fluorescence efficiency in the doped scintillator films.

I. INTRODUCTION

Doped organic scintillators have found widespread applications in many domains, such as high energy dosimetry [1–3], ionizing radiation detection [4–6], and organic light emitting devices [7–9]. Organic scintillator films can be fabricated by bulk polymerization, or by spin coating from a solution containing polystyrene (PS) or polyvinyl toluene (PVT) as a base and a small fraction of fluorophore dopants as active scintillators [4,7], such as 2,5-diphenyloxazole (PPO) or p-terphenyl (PTP) and 1,4-bis(5-phenyl-2-oxazolyl)benzene (POPOP) (POPOP is often used as a tertiary scintillator). Upon bombardment by ionizing particles, electron-ion pairs are generated within the matrix [10–12], and the ionized molecules undergo Langevin recombination with the electrons to produce excitons [10,13,14]. Subsequently, photons are emitted by exciton decay processes [4,7,15].

Although the response of plastic scintillators in high energies ($\geqslant 1$ MeV) are known for a long time, and applications are ubiquitous [1–9], only recently have there been growing interest in their response to low energies ($\leqslant 1$ MeV) of an ion beam, such as for dose measurements in low-energy radiology applications [16–20], radioactive ion beam (RIB) applications [21,22], and detection of nuclear recoil of weakly interacting massive particle (WIMP) dark matter [5,10]. It is generally observed that the scintillation yield (i.e., photons generated from a single incident ion) per unit ion energy is significantly lower for low energy incident ions (<1 MeV) [10,11,16–20] than for high energy ions; however, very little is known about the mechanisms of ionoluminescence (IL) and spectral characteristics at sub-MeV energies. To our knowledge, the effect of ion-flux density on the yield has not been investigated for steady-state characterization of the scintillators. Also, irradiation induced damage of the plastic scintillators leads to gradual decrease of IL yield with increasing dose [4,6]; and their possible effect on the excited state densities are not yet thoroughly explored.

We report on experimental results on steady-state IL measurements from PS based scintillator films at low kinetic energy (50–350 keV) of ion beam. Both pure PS and PS doped with four types of fluorophores have been investigated. The four types of fluorophores used are: (1) POPOP, (2) Coumarin 6, (3) PPO, and (4) PTP. Their photoluminescence properties in PS films have been characterized before [23], and their steady-state absorption and photoluminescence emission spectra are also available in the PhotoChemCad database [24]. The choice of fluorophore doping covers a wide spectrum of aromatic fluorophore types, including auxochromic (Coumarin 6), phenyl (PTP), and oxazole (one and two in PPO and POPOP, respectively) substitutions, with a wide range of absorption wavelengths that allow different energy transfer efficiencies from PS to the fluorophores. In this work we have measured IL from these scintillator films, induced by singly charged positive helium (He$^+$) ions (mass over charge ratio $= 4$ amu/q, q being electronic charge) of different kinetic energies and flux densities. A model combining various mechanisms for scintillation generation and quenching has been developed and compared with the experimental data to understand the dependence of IL yields on the beam current density, irradiation induced damage, and energy.

II. SAMPLE PREPARATION

The scintillator films are prepared by dissolving the powdered fluorophores and polystyrene in toluene and spin coating on a silicon (Si) wafer [23]. In every 10 ml of toluene, 3 g of polystyrene are dissolved, and different masses of the fluorophores, as described in Table I by the fluorophore to PS mass ratio 1:m, are added. The solution is spin coated on a 50 mm diameter Si wafer at 4000 rotations per minute (rpm). Thickness of the films is above 10 μm for all the samples. The molecular weight M_{PS} and M_{SS} of PS and the fluorophores (i.e., secondary scintillator), and their densities, ρ_{PS} and ρ_{SS}, respectively, are also furnished in Table I.

III. IONOLUMINESCENCE MEASUREMENTS

The IL measurement setup consists of an ion-irradiation assembly, an optical fiber-integrated charge coupled device (CCD) spectrometer, and an ion implantation chamber. A

*Corresponding author: Mhuang@sunypoly.edu

TABLE I. Composition and physical properties [25] of the different scintillator films with PS as the primary scintillator.

Scintillator film type	Fluorophores[a] (Secondary scintillator)	Scintillator mass ratio (Secondary: Primary) (1:m)	Molecular weight (g/mol) of		Density (g/cm^3) of	
			Primary (M_{PS})	Secondary (M_{SS})	Primary (ρ_{PS})	Secondary (ρ_{PS})
1	None	–	104.2	–	0.9 ± 0.1	–
2	POPOP	1/3000	104.2	364.4	0.9 ± 0.1	1.2 ± 0.1
3		1/300				
4	Coumarin 6	1/300	104.2	350.4	0.9 ± 0.1	1.3 ± 0.1
5		1/30				
6	PPO	1/100	104.2	221.3	0.9 ± 0.1	1.1 ± 0.1
7		1/10				
8	PTP	1/100	104.2	230.3	0.9 ± 0.1	1.0 ± 0.1
9		1/10				

[a]Purchased from Sigma Aldrich (https://www.sigmaaldrich.com/).

schematic of the light collection efficiency of our setup is shown in Fig. 1.

An optical fiber of core diameter $D_f = 600 \, \mu$m and numerical aperture $N_A = 0.36$ is placed at a distance $L = 3$ mm from the sample plane at an angle $\theta_f = 45°$. The fiber has an elliptical acceptance area $A_a \approx 4.5 \, \text{mm}^2$ due to the angular alignment, which is completely inscribed within the 7 mm^2 circular irradiation area. Polystyrene has a refractive index $n_{PS} \approx 1.55$, transmitivity $\approx 95\%$, and a critical angle of refraction $\theta_C \approx 42°$ not considering its chromatic dispersion. Therefore from a uniform emission over the entire 4π steradian solid angle from all scintillator sites within area A_a and the projected range of the impinging ion in PS d_h, the average fraction of the emission that comes out of the film is approximately $0.95 \times (1 - \cos\theta_C)/(2\pi) = 3.90\%$, where $2 \times (1 - \cos\theta_C)$ is the solid angle inscribed within the critical angle θ_C. If we assume that the externally emitted photons are uniformly distributed over the 2π steradian solid angle above the sample, the fraction of external emission captured by the fiber is approximately 0.25%. The optical fiber and the feedthrough have a combined transmissivity of approximately 72.90%. Therefore, the collection efficiency of the system is

obtained by multiplying these three factors and is approximately $g \sim 0.007\%$ from the total emission from area A_a.

In order to measure the entire emission spectra from a film within a predefined integration time, we use a CCD spectrometer QEPro from *OceanOptics* [26] having a wavelength range $\lambda_{min} = 200$ nm to $\lambda_{max} = 1000$ nm. The spectrometer has a Hamamatsu S7031-1006 scientific grade, back-thinned CCD detector array (1044×64 pixels) [27]. It has a minimum 8 ms integration time, well capacity of 200 000 photoelectrons/pixel, 0.8 ms dead time before initialization of the charge integration, and another 1.2 ms data acquisition and transfer time when buffering is enabled (buffer capability 15 000 spectra), making a total 2.0 ms effective dead time between successive integration periods [28]. During the experiments, the integration time T_{int} is always above 10 s, and the photoelectrons counted during the experiments are below 10 000 counts/pixel in all integration times, much lower than the well-saturation limit. Therefore the photoelectrons not captured during the much smaller dead time are ignored. The quantum efficiency of the CCD is above 80% between 500 and 800 nm [27]. The spectral nonlinearity of the CCD response and its nonlinearity with light intensity are precalibrated and are taken into account by enabling a sixth-order polynomial nonlinearity correction in the driving software (Oceanview) while reading CCD counts [28]. An in-built thermoelectric (TE) cooler in the spectrometer can cool the CCD to about $T_{TEC} = -20 \,°$C. The initial calibration of the spectrometer showed a dark rate of approximately 2 counts/s pixel^{-1} at this temperature (see the Supplemental Material [29] for more details). After the integration time T_{int} is fixed, dark count subtraction is performed for all spectral measurements, producing a root mean squared (rms) noise floor of ± 0.2 counts/s pixel^{-1}. Since $\lambda_{max} \geqslant 2\lambda_{min}$ for the spectrometer, the CCD pixel illuminated by the first order principal peak of a wavelength λ is also illuminated by the second order principal peak of the wavelength $\lambda/2$. We have observed that amplitude of this second order peak between 400 and 1000 nm is nearly $24\% \pm 6\%$ of the corresponding first order peak between 200 and 500 nm and hence in all spectral measurements, 24% of the counts between $200 \leqslant \lambda \leqslant 500$ nm are subtracted from the counts between $400 \leqslant \lambda \leqslant 1000$ nm as a corrective measure (see the Supplemental Material [29]
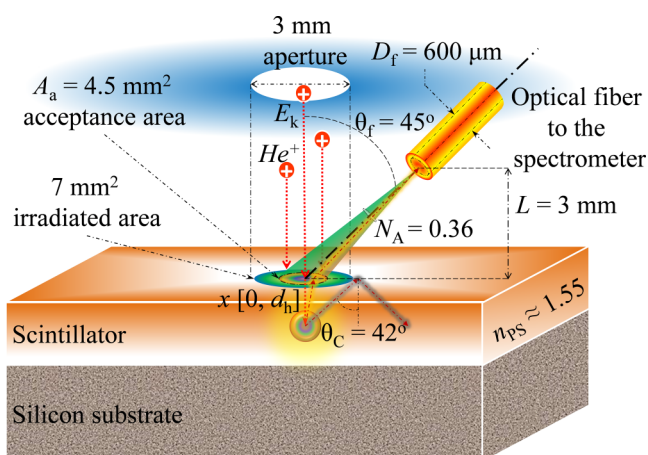

FIG. 1. A schematic of the ionoluminescence measurement setup (not to scale). The ionoluminescence is recorded with an optical fiber integrated spectrometer.

for more details). We compared the power calculated from the spectral counts of the spectrometer and the true power measured with a powermeter (Newport model 1916-C [30]) in identical conditions from a programmable monochromatic source between 350 and 950 nm and found a ratio of 0.87 ± 0.07 between them (see the Supplemental Material [29] for more details). This indicates that the yield calculations, assuming the counted photoelectrons from the spectrometer to be the actual incident photon counts, would lead to a 13% uncertainty. This uncertainty is much lower than the experimental errors estimated in Sec. V from IL measurement of undoped and doped PS films.

For ionoluminescence measurements, He$^+$ ions are generated from a plasma in an ion implanter operating between 50 and 350 keV (Extrion Ion Implanter, Ion Beam Laboratory, University at Albany). After being mass selected and extracted from the ion source, the He$^+$ ion beams are electrostatically steered and square-rastered over an area of ~ 50 mm in diameter. With an electropneumatically controlled shutter, the beam is allowed to implant on the sample through a 3 mm diameter aperture. The average ion current densities are controlled in the range of 1–300 nA/cm^2 by tailoring the plasma discharging conditions (e.g., helium gas pressure and ion source arc voltage). Due to the rastering scheme of the ion implanter, the beam current on the sample varies in a raised sinusoidal form with about 100 ms repetition period (see the Supplemental Material [29] for more details). We show in the Supplemental Material [29] that, since the integration period in the experiments is always above 10 s, much higher than the 100 ms repetition period of the beam current, the beam current density can be considered to be practically constant at its mean value J with negligible error, for steady-state response analysis of the samples. Therefore, the following analysis of photon yield is based on the assumption of constant beam current density J and the approximation closely represents the steady-state response of the samples, had the current density been actually constant at J.

IV. THEORETICAL MODEL

A. Exciton generation

There are several models [5,31–34] to evaluate L_m, the number of excitons generated from the distinct ion track of a single incident particle. Chou's empirical model [1,32,34] is often used over a large range of incident kinetic energies, given by

$$L_m(E_k) = L_a \int_0^{E_k} \frac{dE}{\left[1 + kB\left(\frac{dE}{dx}\right) + C\left(\frac{dE}{dx}\right)^2\right]}, \quad (1)$$

where dE is the loss of kinetic energy in traversing a distance dx through the sample. Here kB (Birk's parameter) and C are constants, usually evaluated from empirically fitted data and are considered independent of the type of particles or their total stopping power dE/dx. L_a is the absolute scintillation efficiency, defined as number of excitons generated per unit incident energy of a single ion and is assumed to be a constant over all energies, and L_m approaches $L_a E_k$ only when irradiating particles have a very low total stopping power, where the first order and second order terms in the denominator of Eq. (1)

are negligible compared to unity. For organic scintillators, typical values of $L_a \approx 8$–10 excitons/keV [21,35]. However, these values are usually valid at above 1 MeV kinetic energies and at lower energies, the validity of these values are debatable [19,33]. For high total stopping powers, the high ionization density core of the ion track behaves as a quenching species to trap the generated excitons, resulting in a reduction of the scintillation yield L_m from the asymptotic value $L_a E_k$. At high energies, typically for $E_k \geqslant 1$ MeV for ions, or $E_k \geqslant 100$ keV for electrons, Eq. (1) reduces to Birk's law [1,5] with $C \approx 0$ and L_a representing the actual absolute yield. Depending on the experimental setup, energies, and ion types used, a wide range of values of kB has been reported for PS, between 3.4 [19] and 13.5 mg/cm^2 MeV^{-1} [11].

However, at $E_k \leqslant 1$ MeV for ions, the applicability of Birk's law with a constant kB (and $C = 0$) is debatable [10,11,17,34,36–39] and the yield L_m is significantly lower than that predicted using the value of kB obtained at high energies. At low energies, significant nuclear recoils result in more translational motion and damage of the scintillator molecules [10,31,38]. Lindhard correction [10] on L_a is often used in tandem with Birk's law to take into account the reduction of yield due to nuclear recoils, by multiplying L_a with a quenching factor determined by the nuclear to the total stopping power ratio. Also, high ionization density at low kinetic energies (typically $\leqslant 1$ MeV) results in a significant number of electrons escaping the Langevin recombination process, thus generating fewer excitons. Experiments and calculations have shown that the measured scintillation yields with low-energy incident ions [10,11,38] are one to two orders of magnitude lower than that predicted by Birk's law. Boivin *et al.* [17] showed an $E_k^{-1/2}$ dependence of kB using 1–1000 keV proton beams for PS-based scintillating fibers. Chou's model in Eq. (1), on the other hand, provides an extra degree of freedom in the fitting process by introducing the constant C without accommodating a corrected L_a. In Table II a list of scintillation yield measurements based on Birk's law and Chou's model for plastic scintillators are furnished from literature for ion energy up to $E_k = 1000$ keV. It can be seen that the measured kB and C values vary over a wide range, depending on the type and energy of charged particles. Moreover, not much information is available on the absolute value of L_a at these low energies, because yield measurements are often performed relative to a known reference (e.g., electrons at a particular high energy) in identical conditions [5,31]. In the last column of Table II, reported L_a values are listed from only those references [19,33] where total emission measurements have been performed.

In Fig. 2(a) the total stopping powers of He$^+$ ions in PS, dE/dx, and the projected range d_h, simulated using the Stopping and Range of Ions in Matter (SRIM) software [40], are shown between initial kinetic energy range 1–500 keV. The error bar on the projected range represents the longitudinal straggle, also evaluated from SRIM simulation. In Fig. 2(b) the yield L_m is calculated from Eq. (1) using the simulated dE/dx values and the values of L_a, kB, and C listed in Table II for PS using Frelin's [19] and Tadday's [33] data. The shaded region in Fig. 2(b) indicates the range of yields calculated for three different PS-based scintillators in Frelin's work [19]. It can be seen that the projected range is much smaller than the thickness

TABLE II. List of reported scintillation yield measurements from plastic scintillators ($E_k \leqslant 1$ MeV).

Reference	Primary Scintillator	E_k range (keV)	Charged particle	Model	kB (mg/cm^2 MeV^{-1})	C (mg/cm^2 MeV^{-1})^2	L_a (excitons/keV)
Reichhart et al. [11]	PS	300–850	electron	Birk	13.5	0	–
Frelin et al. [19][a,b]	PS	1–90	electron	Birk	3.4 ± 0.3	0	0.84 ± 0.02
					5.3 ± 0.5	0	1.80 ± 0.01
					6.8 ± 0.7	0	2.25 ± 0.01
Boivin et al. [17]	PS	1–1000	proton	Birk	$69 \times E_k^{-1/2} - 2.7$	0	–
Tadday [33][b]	PS	1–140	electron	Chou	13.3 ± 6.9	71.9 ± 12.0	29.49 ± 0.87
Craun and Smith [39]	PVT	350–15 000	proton	Chou	12.9	10.1	–
Frelin et al. [19]	PVT	1–90	electron	Birk	5.6 ± 0.6	0	2.52 ± 0.02
					6.4 ± 0.6	0	2.75 ± 0.02
					9.4 ± 1.0	0	2.31 ± 0.03

[a]The three values of kB and L_a reported in [19] correspond to three different commercial PS-based scintillators, respectively.
[b]Used for further analysis for the PS-based samples and also used in Fig. 2(b).

($\sim$10 μm) of the samples described in Sec. II, ensuring that the ions lose their kinetic energy completely in the scintillator film itself. The combination of L_a, kB, and C used by Frelin et al. [19] and Tadday [33] results in similar values of L_m at above 300 keV; however, at lower energies, the values tend to deviate from each other with Tadday's results being about twice the result reported by Frelin et al.

B. Rate equations

When excitons are generated by recombination of the ionized molecules and electrons, spin statistics suggests that the number of generated singlets is $\frac{1}{3}$ of that of triplets [13,14,41]. Therefore, for an incident ion current density J (from here onwards, current density is assumed constant based on discussion in the previous section) if all the ion tracks are well separated, and Eq. (1) is satisfied for individual ion tracks, the rate of electrical generation of singlet and triplet excitons per unit volume can be written as $\frac{1}{4}(\frac{JL_m}{qd_h})$ and $\frac{3}{4}(\frac{JL_m}{qd_h})$, respectively. The deexcitation from excited states may take several radiative and nonradiative pathways, with only the radiative decay leading to photon emission. At high excitation intensities and small intermolecular distances, singlet-singlet annihilation (SSA) and triplet-triplet annihilation (TTA) mechanisms, by means of Förster resonance energy transfer (FRET) or Dexter transfer between spatially correlated neighboring

excited molecules, may also take place. If $2N_S$ singlet excitons (N_S is a large integer) participate in SSA, N_S of them completely transfer their energy to the other N_S excitons and come to ground state nonradiatively. Hence, the rate of loss of singlet excitons by SSA is $\frac{1}{2}$ of the rate at which a singlet exciton participates in SSA. The threefold spin multiplicity of triplet states dictates that such biexcitonic annihilation of triplet excited states (TTA) may result in triplet as well as up-converted singlet exciton in the same ratio 3:1. Therefore, if $2N_T$ triplet excitons (N_T is a large integer) participate in the process, $\frac{3}{4}N_T$ triplet excitons and $\frac{1}{4}N_T$ singlet excitons are generated; while the rest N_T decay nonradiatively. Hence the loss rate of triplets is $\frac{5}{8}$, and the generation rate of singlets is $\frac{1}{8}$, of the rate at which a triplet exciton participates in TTA.

Several other loss mechanisms, such as singlet-triplet annihilation (STA), singlet-polaron, and triplet-polaron recombination may also take place in the films [13,14]. We observe by experiments in Sec. V that the saturation value of triplet density is nearly proportional to J and saturation singlet density increases as an increasing parabolic function of J. This leads to a linearly increasing variation of singlet ionoluminescence yield with increasing J. We show later in Sec. V B, Eq. (16), that inclusion of STA does not explain this linear dependence of the singlet yield, rather it shows a decreasing trend with increasing current density. Hence we assume in the model that the STA rate is negligible. The ion irradiation on
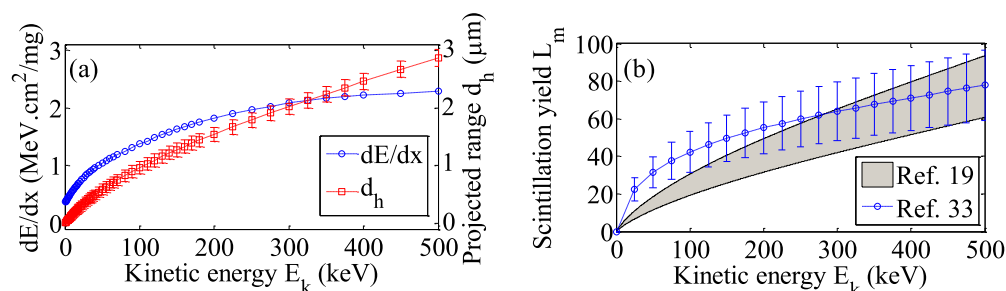

FIG. 2. (a) SRIM-simulated total stopping power dE/dx and projected range d_h of He$^+$ ion in PS as a function of its initial kinetic energy E_k. The error bar on d_h represents the longitudinal straggle. (b) Calculated yield L_m in PS scintillators for the He$^+$ ion based on Eq. (1) with L_a, kB, and C values listed in Table II. The simulated dE/dx from (a) is used in Eq. (1) to find L_m by numerical integration. Only results reported by Frelin et al. [19] and Tadday [33] are plotted. Frelin et al. [19] used three PS-based scintillators and the shaded region covers the upper and lower limit of expected values of L_m.

nonconductive films can also produce space-charge polarons that absorb singlet or triplet excitons at a rate proportional [13] to $\sqrt{J}$, not explaining the J^2 dependence of singlet density. As a result, we have considered only SSA and TTA in our model and the other biexcitonic annihilation mechanisms are ignored. We further assume that the triplet generation rate by intersystem crossing is negligible compared to the electrical generation rate of triplets [13], as the flux density is high and intersystem crossing rate is usually very low. We show later that only TTA leads to a J^2 dependence of the density of singlet states that describes our experimental observations.

The irradiation-induced damage of scintillator sites has different effects on singlet and triplet yields. Prolonged ion irradiation on PS films permanently damages the scintillation sites by formation of polycyclic aromatic hydrocarbons (PAH) and reactive radicals [8,9] by dissociation of its aromatic and aliphatic C–H bonds, C–C bonds, and the pendant groups, capable of bonding with each other, and behaving either as an exciton quencher or triplet emission source (color centers). The total rate of such damage creation of the primary scintillator molecules is proportional to the ion current density J. All these damaged or PAH sites act as static quenching traps for singlet excitons because they are no longer capable of emitting like pristine PS. However, a fraction (k_T) of them may, in general, act as triplet color sources and the rest ($1 - k_T$) as triplet quenchers. Therefore, the quenching "half-life," that is the time required to reduce the emission intensity of the singlet and triplet excitons by 50% of that of pristine scintillator, can be written as

$$t_f = \frac{q d_h N_{PS}}{2 L_D J} \tag{2a}$$

and

$$t_p = \frac{t_f}{(1 - k_T)}, \tag{2b}$$

respectively, where the initial density of pristine PS molecules is N_{PS} ($\approx 5.8 \times 10^{21}/\text{cm}^3$) and L_D is the number of damaged sites generated by a single ion which is expected to be of the level of $L_a E_k$ or higher. The most commonly used empirical model for damage-induced quenching of excitons is given by the Birk-Black model [42,43] that predicts the exciton quenching factor as a function of time t in terms of the half-life as

$$Q_S(t) = \left(1 + \frac{t}{t_f}\right)^{-1}, \tag{3a}$$

$$Q_T(t) = \left(1 + \frac{t}{t_p}\right)^{-1} \tag{3b}$$

for the singlet and triplet emission, respectively. Therefore considering all these mechanisms and assumptions, if $n_S(t)$ and $n_T(t)$ are singlet and triplet exciton densities at time t, the rate of increase of singlet and triplet exciton can be written, respectively, as

$$\frac{dn_T}{dt} = \left(\frac{3}{4} L_m + k_T L_D\right)\left(\frac{J}{q d_h}\right) Q_T(t) - \left(\kappa_T + \kappa_{NR}^T\right) n_T$$
$$- \frac{5}{8} \kappa_{TT} n_T^2, \tag{4a}$$

$$\frac{dn_S}{dt} = \left(\frac{1}{4} \frac{L_m J}{q d_h} + \frac{1}{8} \kappa_{TT} n_T^2\right) Q_S(t) - \left(\kappa_S + \kappa_{NR}^S\right) n_S$$
$$- \frac{1}{2} \kappa_{SS} n_S^2. \tag{4b}$$

Here κ_T (κ_S), κ_{NR}^T (κ_{NR}^S), and κ_{TT} (κ_{SS}) are the triplet (singlet) radiative rate, triplet (singlet) nonradiative rate, and TTA (SSA) rate, respectively. Equations (4a) and (4b) form a pair of Riccati equations and cannot in general be solved to find the analytical expressions of n_S and n_T due to the time dependent factors Q_S and Q_T. Therefore, what follows in Sec. V is a semiempirical analysis of the test results and application of these state equations (4a) and (4b) specific to the scintillators.

V. EXPERIMENTAL RESULTS

A. Triplet emission of pure PS

Figure 3(a) shows the uncorrected IL spectra of pure PS samples as a function of irradiation time at $E_k = 350 \text{ keV}$. The counts are normalized by the peak counts at 320 nm obtained between 0 and 10 s integration time.

Two emission bands are clearly distinguishable. The intensity of the higher energy band, between $250 \leqslant \lambda \leqslant 400 \text{ nm}$, with a peak at $\lambda_{em}^{PS} = 320 \text{ nm}$, falls off sharply with increasing irradiation time; however, the intensity of the broad lower energy band, between $450 \leqslant \lambda \leqslant 800 \text{ nm}$, reduces by a much smaller value over the entire irradiation duration. Similar results were reported by Kim et al. [9] with ultraviolet (UV) pulsed excitation. The wavelength range of the high energy band resembles the UV fluorescence emission spectra of PS [8,9,44] and hence can be identified as the singlet (S*) emission band. The low energy band resembles the sustained white-light emission from the PAH sites reported by Kim et al. [9] and Lee et al. [8] and is identified as the triplet (T*) band [45]. The error bars, shown at a regular interval of 25 nm, are evaluated by the standard deviation of $0.2 \text{ counts/pixel s}^{-1}$ obtained after the dark-count correction discussed in Sec. III. This is representative of the signal-to-noise ratio of our measurements.

As discussed in Sec. III, a second principal peak at 640 nm is observed between the 0 and 10 s integration period, which is the second order principal peak of the spectrometer corresponding to the strong singlet peak at 320 nm. This artifact band overlaps with the triplet band of emission. Since the singlet peak diminishes rapidly over subsequent integration intervals, the corresponding artifact peak is not observable after 10 s. However, a correction is employed, by subtracting 24% of the counts between $200 \leqslant \lambda \leqslant 500 \text{ nm}$ from the counts between $400 \leqslant \lambda \leqslant 1000 \text{ nm}$, to eliminate this artifact from the triplet band as discussed in Sec. III. In Fig. 3(b) the uncorrected and corrected spectra are shown for comparison at selected integration intervals of 0–10 s, 10–20 s, and 70–80 s. It can be seen that the corrected spectra follows the as-measured spectra as the singlet emission diminishes with increasing irradiation time.

In Fig. 4(a) the total number of photons measured by the spectrometer in successive integration periods are shown at different constant beam current densities J. The data corresponding to singlet and triplet band are separately evaluated by summing the measured photons in the bands $250 \leqslant \lambda \leqslant$
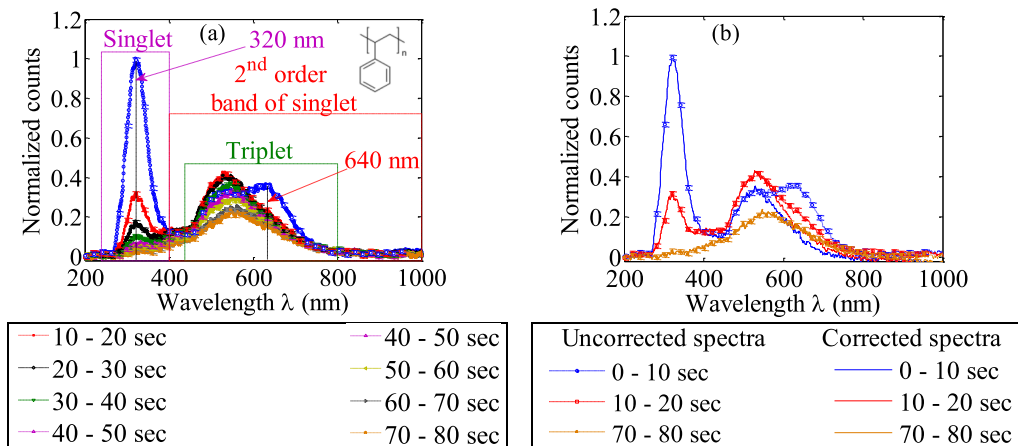
FIG. 3. (a) Measured emission spectra (uncorrected) of pure PS film at different integration periods. The emission band between $250 \leqslant \lambda \leqslant 400$ nm is identified as a singlet band (fluorescence) and the band between $450 \leqslant \lambda \leqslant 800$ nm is identified as a triplet band (phosphorescence). Kinetic energy $E_k = 350$ keV, current density $J = 215$ nA/cm^2. The region between $400 \leqslant \lambda \leqslant 1000$ nm is the second order principal diffraction affected zone of the spectrometer (see the Supplemental Material [29] for more details). A peak is observed at 640 nm which is the second order principal peak corresponding to the primary singlet peak at 320 nm. The error bars are shown at a regular interval of 25 nm and they represent the 0.2 counts/pixel s^{-1} noise floor of spectral measurements. (b) Spectral correction by removing the second order principal diffraction artifact from the measured counts. Dashed lines with error bars on them are the uncorrected spectra at some selected integration intervals (described in the legends) and the continuous lines in the same color are the corresponding corrected spectra.

400 and $450 \leqslant \lambda \leqslant 800$ nm, respectively. The error bars are calculated from the rms noise floor of 0.2 counts/pixel s^{-1}. Typical values of the error bar are less than 1% for the singlet band and 7% for the triplet band at their respective highest

values shown in Fig. 4(a). The difference is due to ~2.3 times higher bandwidth and ~2.5 times lower peak counts/pixel in the triplet band in the first integration period. The singlet and triplet counts are marked with hollow and filled data markers,
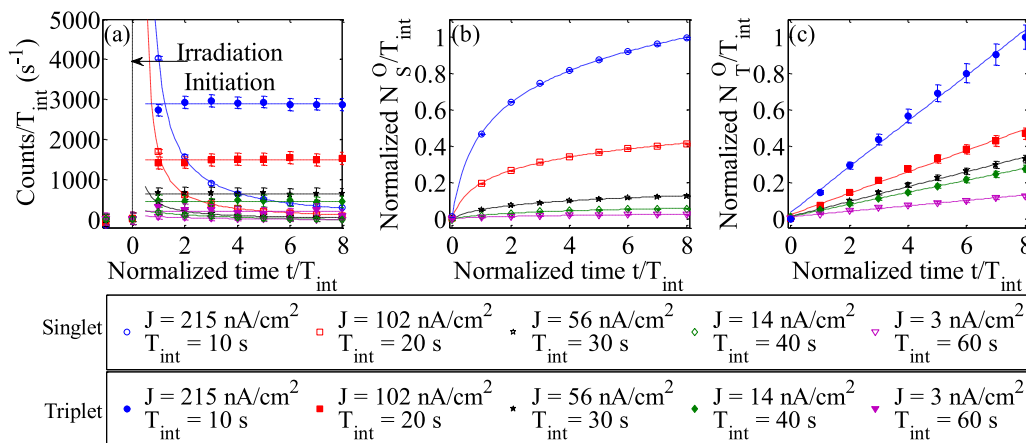

FIG. 4. (a) Measured counts of the spectrometer as a function of iradiation time, both normalized by the integration time T_{int}. Five different beam current densities are used between $J = 3$ and 215 nA/cm^2. The integration time and respective current densities are listed in the figure legends. The hollow data markers are for the singlet band, between $250 \leqslant \lambda \leqslant 400$ nm, and the filled data markers are for the triplet band, between $450 \leqslant \lambda \leqslant 800$ nm. Ion beams are initiated at $t = 0$, whereas the counts recorded before ion initiation correspond to the dark counts. The singlet emission intensity falls off sharply following the Birk-Black model given in Eq. (3a), whereas the triplet counts remain more or less constant over the duration of irradiation. The dashed lines represent the respective fitting lines, i.e., Birk-Black fitting for singlets and constant values for triplets. The first available data set corresponding to the IL response is between $t = 0$ and T_{int} and is available at $t = T_{int}$. The fitting of the singlets to the Birk-Black model using the spectrometer counts is inaccurate to estimate by extrapolation the count rate at $t \rightarrow 0+$ due to discontinuity of the function at $t = 0$. Fitting the time integral of the Birk-Black model to integrated photon counts alleviates this issue. Integrated number of photons emitted per unit area of the scintillator are shown in (b) for singlet and (c) for triplet band, respectively, as a function of time, both normalized by integration time. The integrated counts are further normalized by the value obtained at $J = 215$ nA/cm^2 and $t = 8T_{int}$ in each case. The total number of photons are obtained by first integratng the recorded counted in the singlet (a) and triplet (b) bands separately and then integrating over the irradiation time 0 to t. The dashed lines in (b) represent a logarithmic fitting of singlet density as described later by Eq. (9) and is discussed in Sec. V B. Triplet density is fitted linearly shown by dashed lines in (c), which is equivalent to the mean value plot of triplets shown in (a). Kinetic energy $E_k = 350$ keV in all cases.

respectively. Both time and the counts are normalized by the respective integration times T_{int} to display them on the same scale. Irradiation is initiated at time $t = 0$ while the counts recorded before that correspond to dark counts. The IL data corresponding to the first T_{int} duration of irradiation is available at $t = T_{int}$ and so on. It can be noted that the singlet counts fall off sharply with time, whereas the triplet rate remains more or less constant. We will show in Sec. V B that the singlet counts can be fitted to the Birk-Black model of quenching given in Eq. (3a) to find the IL yield at $t = 0$. Howerver, to obtain the counts rate immediately after starting irradiation would require extrapolating the singlet plots to $t \rightarrow 0$, where the singlet emission plot passes through a discontinuity, i.e., $n_S(t \rightarrow 0-) = 0 \neq n_S(t \rightarrow 0+)$, $0-$ and $0+$ being usual symbol of limiting values at $t = 0$ from the ranges $t \leqslant 0$ and $t \geqslant 0$, respectively. It would, therefore, be more fitting convenient to evaluate the integrated counts $N_S^O(t)$ and $N_T^O(t)$ for singlet and triplet bands, respectively, over time t, and then fitting to the integrated Birk-Black model, because $N_S^O(t \rightarrow 0-) = 0 = N_S^O(t \rightarrow 0+)$. Here $N_S^O(t)$ and $N_T^O(t)$ are defined as

$$N_S^O(t) = d_h \kappa_S \int_{t=0}^{t} n_S(t) dt \qquad (5a)$$

and

$$N_T^O(t) = d_h \kappa_T \int_{t=0}^{t} n_T(t) dt, \qquad (5b)$$

respectively. $N_S^O(t)$ and $N_T^O(t)$ are calculated by adding the measured counts shown in Fig. 4(a) up to time t. Both these values are normalized by the value obtained at $t = 8T_{int}$ with $J = 215 \, \text{nA/cm}^2$. At low J, the rate of exciton generation is low and thus the integration time is set to higher values.

In this section we only consider the triplet emission in Fig. 4(c) and the singlet emission in Fig. 4(b) will be discussed in Sec. V B. The triplet integrated counts in Fig. 4(c) are fitted to a linear equation in the MATLAB curve fitting tool [46] with two adjustable parameters. The slope of the fitted equation represents the triplet exciton density and the offset takes into account the nonzero dark counts. The reduced Chi-squared values (χ^2) of the linear fitting process are obtained as 0.26–0.69 as current density J is decreased, indicating a good fit. The linear dependence of the triplet emission on the integration time indicates that triplet density n_T reaches a steady-state value $n_{T\infty}$ within the first few seconds of irradiation. It can be seen from Eq. (3b) that the triplet static quenching factor Q_T with a finite value of triplet half-life t_p leads to a steady-state value $n_T(\infty) = 0$, because over prolonged irradiation, all the molecules eventually would stop emitting. The data suggest that the irradiation induced damage of pristine PS molecules leads mostly to emissive PAHs, i.e., the fraction $k_T \approx 1$ in Eq. (3b), and the triplet static quenching by damage is negligible, i.e., $Q_T \approx 1$. Under this condition, the transient solution of Eq. (2a) results in

$$n_T(t) = n_{T\infty} \frac{(1 - e^{-f_T t})}{\left[1 + \left(\frac{\Delta_T - 1}{\Delta_T + 1}\right) e^{-f_T t}\right]}, \qquad (6)$$

where

$$\Delta_T = \sqrt{1 + \frac{J}{J_T}}, \qquad (7a)$$

$$\left(\frac{1}{J_T}\right) = \frac{5}{2q d_h} \left(\frac{3}{4} L_m + L_D\right) \tau_T^2 \kappa_{TT}, \qquad (7b)$$

$$\tau_T = \left(\kappa_T + \kappa_{NR}^T\right)^{-1}, \qquad (7c)$$

$$f_T = \Delta_T \left(\kappa_T + \kappa_{NR}^T\right), \qquad (7d)$$

$$n_{T\infty} = n_T(\infty) = \frac{4}{5 \tau_T \kappa_{TT}} (\Delta_T - 1). \qquad (7e)$$

Here we define the term J_T for brevity which has a unit of current density and τ_T is triplet lifetime. Equation (7e) gives the expression for the steady-state triplet density reached in Fig. 4(c) which is the slope of the linearly fitted results. Phosphorescence lifetime of PS can be considered as $\tau_T \sim 100 \, \mu\text{s}$ [47,48]. A typical value of κ_{TT} for polymers is [14] between 10^{-14} and $10^{-11} \, \text{cm}^3/\text{s}$ leading to $\tau_T^2 \kappa_{TT}$ between 10^{-22} and $10^{-19} \, \text{cm}^3 \, \text{s}$. For $E_k = 350 \, \text{keV}$, $L_m \approx (75 \pm 15)$ and $L_m \approx (60 \pm 10)$ can be calculated from Fig. 2(b) using Tadday's and Frelin's data, respectively, and $d_h \approx (2.2 \pm 0.1) \, \mu\text{m}$ is obtained from Fig. 2(a). We assume for simplicity $L_D \sim E_k L_a \approx 10^3$, leading to $J_T \approx 14 \, \text{nA/cm}^2$ to $13.8 \, \mu\text{A/cm}^2$. The current densities used in our experiments are within the range $1 \leqslant J \leqslant 250 \, \text{nA/cm}^2$, i.e., $J \ll J_T$ for the lower values of J, although the same may not be valid at the higher values of J. We will show in the next section that our measured value of $\tau_T^2 \kappa_{TT}$ is between 0.10×10^{-21} and $0.34 \times 10^{-21} \, \text{cm}^3 \, \text{s}$, well within the expected range of $\tau_T^2 \kappa_{TT}$ and $J_T \geqslant 1.0 \, \mu\text{A/cm}^2$ satisfying $J_T \gg J$. Therefore we make a small value approximation of J/J_T in Eq. (7a), and the triplet density would vary as Eq. (9) to reach a steady-state value, approximated from Eq. (7e) as

$$n_{T\infty} \approx \frac{2}{5 \tau_T \kappa_{TT}} \left(\frac{J}{J_T}\right) \qquad (8)$$

within a time much shorter than the sampling period (T_{int}) of our IL data. Hence the observed triplet density $n_{T\infty}$ is expected to approximately follow a linear relationship with current density J. In Fig. 5 the normalized triplet density (normalized by its measured value at $E_k = 350 \, \text{keV}$ and $J = 215 \, \text{nA/cm}^2$) $n_{T\infty}$ is plotted against current density J at three different kinetic energy values and fitted as a linear function of J. The fitting produces a reduced Chi-squared value (χ^2) of 1.14, 1.16, and 1.48 at energies 350, 150, and 50 keV, respectively, indicating a moderate fit. The proportionality constant increases with the ion energy E_k. Similar linearity was reported by Jiménez-Rey et al. [49] between emission intensity and beam current density using phosphor screens in sub-100 keV energies, where the emission was essentially from excited triplet states. The nonzero offset of the $n_{T\infty}$ vs J plots may be associated with the fitting errors. We find that an uncertainty $\pm 50\%$ in the nonzero offset leads to a change of $\sim \pm 4\%$ in the slope of the plots. This is well below the estimated fitting errors shown as an error bar in Fig. 5.
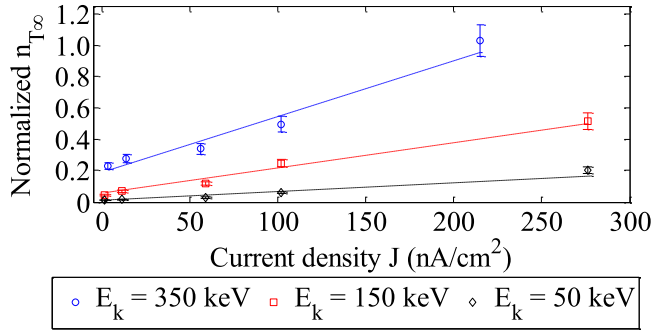
FIG. 5. Normalized saturation triplet density $n_{T\infty}$ vs current density J for pure PS film. Saturation triplet exciton density $n_{T\infty}$ is evaluated by finding the constant slope of Fig. 4(c) by a linear fit. Value of $n_{T\infty}$ with $J = 215$ nA/cm^2 and energy $E_k = 350$ keV is used as the normalization factor. The error bars show the error limit on these constant slopes obtained by linear fit. The dashed lines represent a linear fitting between $n_{T\infty}$ and J.

B. Singlet emission of pure PS

Singlet emission occurs on a much shorter time scale than triplet emission. Therefore, singlet density n_S would reach a steady-state value $n_{S\infty}$ within a few ns to μs, before the singlet quenching by irradiatiation becomes effective. Using $n_T = n_{T\infty}$ and $Q_S = 1$ in Eq. (4b), an expression for steady-state singlet density can be found as

$$n_{S\infty} = n_S(\infty) = \frac{1}{\tau_S \kappa_{SS}}(\Delta_S - 1), \qquad (9)$$

where

$$\Delta_S = \sqrt{1 + \left(\frac{J}{J_{SS}}\right) + \left(\frac{J}{J_{ST}}\right)^2}, \qquad (10a)$$

$$\left(\frac{1}{J_{SS}}\right) = \left(\frac{L_m}{2q\,d_h}\right)\tau_S{}^2\kappa_{SS}, \qquad (10b)$$

$$\left(\frac{1}{J_{TS}}\right) = \frac{1}{5}\left(\frac{\tau_S}{\tau_T}\right)\left(\frac{\kappa_{SS}}{\kappa_{TT}}\right)^{1/2}\left(\frac{1}{J_T}\right), \qquad (10c)$$

$$\tau_S = \left(\kappa_S + \kappa_{NR}^S\right)^{-1}, \qquad (10d)$$

where $n_S\infty$ would have been the steady-state singlet density if there were no irradiation-induced damages. Here, again, we define the terms J_{SS} and J_{TS} for brevity and τ_S is singlet lifetime. Typical values [13,14] of SSA rate $\kappa_{SS} \approx 10^{-8}$ to 10^{-11} cm^3/s. Thus, $J_{TS} \sim J_T$, $J_{SS} \gg [J_{TS}, J_T]$ and

$$n_S\infty \approx \frac{1}{2\tau_S\kappa_{SS}}\left[\left(\frac{J}{J_{SS}}\right) + \left(\frac{J}{J_{TS}}\right)^2\right]. \qquad (11)$$

This means that SSA has a negligible effect on the singlet emission at the current densities used in our experiments and the singlet density is expected to increase as a parabolic function of the current density J. If we now consider the irradiation-induced damage, the singlet exciton density is expected to reduce as $n_S(t) = n_S\infty Q_S(t)$ on the observation time scale with $n_{S\infty}$ as an approximate initial value. Hence, the emitted photons per unit area increase nonlinerly with time

as

$$N_S^O(t) = d_h\kappa_S n_{S\infty} \int_{t=0}^{t} Q_S(t)dt = d_h\kappa_S n_{S\infty}t_f\ \ln\left(1 + \frac{t}{t_f}\right). \qquad (12)$$

Therefore, the singlet ionoluminescence yield, i.e., the number of emitted photon per incident ion, also is time dependent. We define a maximum singlet yield Y_{PS} at time $t = 0$ (or after a few singlet lifetimes τ_S) such that the steady-state IL yield would have been Y_{PS} at all times if damage quenching was not present. Y_{PS} can be found using Eqs. (8), (11), and (12) as

$$Y_{PS}(E_k,J) = \eta_{PS}\left[\frac{1}{4}L_m + \frac{1}{8}\frac{\tau_T^2\kappa_{TT}}{q\,d_h}\left(\frac{3}{4}L_m + L_D\right)^2 J\right], \qquad (13)$$

where

$$\eta_{PS} = \tau_S\kappa_S \qquad (14)$$

is the singlet fluorescence efficiency. The maximum photon yield is thus expected to increase linearly with the current density J due to the up-conversion from triplet state by TTA. In the limit $J \to 0$,

$$Y_{PS}(E_k,0) = Y_{PS}^0 = \frac{1}{4}L_m\eta_{PS}. \qquad (15)$$

Torrisi [34] showed an independence of the singlet IL yield $Y_{PS}(E_k, J)$ to current density J by measuring IL intensity as a function of proton beam current density up to $J = 6$ pA/cm^2, much smaller than the current densities used in our experiments. The singlet emission vs time data, shown in Fig. 4(b), is fitted using Eq. (12). The reduced Chi-squared error (χ^2) evaluated for the fitting is 0.14–0.76 as current density is decreased indicating that the incorporation of Birk-Black irradiation induced quenching $Q_S(t)$ in our model well describes the damage progression. From the fitting, the values of the singlet quenching half-life t_f and the product $d_h\kappa_S n_{S\infty}$ are evaluated for finding the singlet yield Y_{PS}.

In Figs. 6(a) and 6(b) the measured Y_{PS} and t_f^{-1} are plotted against the current density J for three different kinetic energies. Singlet yield Y_{PS} shows a linearly increasing dependence on J that can be described by the linear relation in Eq. (13). Inverse of the singlet quenching half-life t_f^{-1} also shows a linear increase with J as predicted by Eq. (2a). Y_{PS} and t_f^{-1} in Fig. 6 are therefore fitted as linear functions of J, from which the zero-current yield Y_{PS}^0 and damages created per ion L_D are evaluated. From the evaluated Y_{PS}^0, fluorescence efficiency η_{PS} is calculated using Eq. (15). Table III presents the various best-fit parameters. Both Tadday's and Frelin's data shown in Table II are used for calculation of L_m, and hence, of η_{PS} and $\tau_T^2\kappa_{TT}$ in Table III. The values calculated using Frelin's data are shown in parentheses immediately below those calculated with Tadday's data. The linear fitting in Figs. 6(a) and 6(b) produce reduced Chi-squared values above 2, indicating that the fitted lines deviate beyond the estimated standard deviations shown in the figures. It can be noted that the standard deviations on the yield Y_{PS} and singlet quenching half-life t_f at different current densities are evaluated from different spots on the sample once the previous spot is completely quenched by prolonged irradiation at a different J and E_k value. The roughness and inhomogeneity
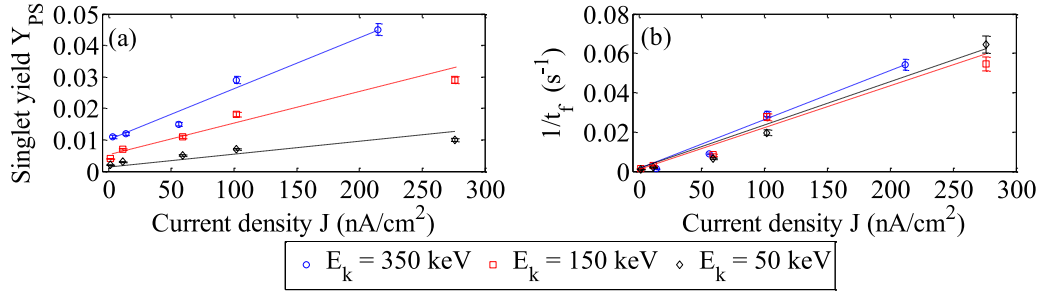
FIG. 6. Evaluated (a) singlet emission yield Y_{PS} and (b) t_f^{-1} vs ion current density J for pure PS samples from measured spectral counts. Logarithmic fitting of singlet emission counts shown in Fig. 4(b) is performed using Eq. (12) at each different current densities J to find t_f and the slope $d_h \kappa_S n_{S\infty}$ at $t = 0$. From the slope, yield Y_{PS} is calculated. The error bar represents the tolerance value on the fitted results. The dashed lines represent the linearly fitted results of variation of yield Y_{PS} and t_f^{-1} with current density J.

of the sample surface, and its composition, if any, have not been evaluated and not included in estimating the standard deviations. However, the general trend of yield Y_{PS} increasing with increasing current density J is indeed the effect of TTA up-conversion that has been proposed in the presented model.

To verify the possibility of other mechanism, such as singlet-triplet annihilation (STA), we look at reported values of STA rate κ_{ST} from literature [14]. Since the contribution of SSA and TTA are governed by the products $\tau_S^2 \kappa_{SS}$ and $\tau_T^2 \kappa_{TT}$, respectively, i.e., the product of the respective rate constants and the lifetimes of the two excitonic species taking part in the biexcitonic process, contribution of SSA, STA, and TTA can be compared by comparing the products $\tau_S^2 \kappa_{SS}$, $\tau_S \tau_T \kappa_{ST}$, and $\tau_T^2 \kappa_{TT}$, respectively. In Table IV typical expected values of these products are compared for polymer materials from literature [14].

$\tau_S^2 \kappa_{SS}$ is significantly lower than $\tau_T^2 \kappa_{TT}$ and is negligible, indicating that SSA requires a much higher ion flux rate than TTA and has been discussed following Eq. (10d). Our estimated value of $\tau_T^2 \kappa_{TT}$ is of the order to 10^{-22} cm^3 s (from Table III) and is within the range of possible values of $\tau_S \tau_T \kappa_{ST}$. Therefore, if STA is included in the rate equations, Eq. (4b) can be modified by adding another term $(-\kappa_{ST} n_S n_T)$ on its right-hand side [13]. Solving the modified Eq. (4b) in the similar fashion for steady-state solution, and using a steady-state value of triplet density $n_{T\infty}$ from Eq. (8), the

singlet yield can be re-evaluated as

$$Y_{PS} \approx \frac{1}{4} L_m \eta_{PS} \frac{\left[1 + \frac{1}{2} \frac{\tau_T^2 \kappa_{TT}}{q d_h} \left(\frac{3}{4} L_m + L_D\right)^2 J\right]}{\left[1 + \frac{\tau_S \tau_T \kappa_{ST}}{q d_h} \left(\frac{3}{4} L_m + L_D\right) J\right]}. \quad (16)$$

For the TTA dominated regime, the numerator in Eq. (16) dominates, where yield Y_{PS} is an increasing function of J, and in the STA dominated regime, the denominator dominates, leading to decreasing Y_{PS} with increasing J. With $\tau_T^2 \kappa_{TT} \sim 10^{-22}$ cm^3 s and damage created per ion $L_D \sim 10^4$ estimated for undoped PS samples $\tau_T^2 \kappa_{TT} L_D^2 \sim 10^{-14}$ cm^3 s, whereas even for the largest possible value of this $\tau_S \tau_T \kappa_{ST}$ from Table IV, $\tau_S \tau_T \kappa_{ST} L_D \sim 10^{-17}$ cm^3 s. Therefore, we believe, the effect of STA is negligible compared to TTA and as a result, singlet yield $Y_{PS}(J)$ is a linearly increasing function of J as seen in Fig. 6(a). This justifies not considering STA in the proposed model.

It can be seen from Table III that the estimated fluorescence efficiency of the undoped PS film increases with kinetic energy based on L_m values taken from Tadday's data, however, it remains close to 0.05% based on Frelin's data. Since fluorescence efficiency is a property of the pristine PS molecules and we do not expect it to change with the kinetic energy of the incident particles, we believe that our PS samples behave more closely to the PS samples used in Frelin's measurements. The measured rate of increase of yield

TABLE III. List of calculated values from fitting of Y_{PS} and t_f^{-1} in Figs. 6(a) and 6(b).

Kinetic energy E_k (keV)	$10^3 \times Y_{PS}^{0}$ [a]	L_m [b]	d_h [c] (μm)	$10^4 \times \eta_{PS}$ [d]	$10^3 \times \left(\frac{\partial Y_{PS}}{\partial J}\right)_{E_k}$ [a] (cm^2/nA)	$10^{-3} \times L_D$ [e]	$L_D/(E_k L_a)$ [f]	$10^{21} \times \tau_T^2 \kappa_{TT}$ [g] (cm^3 s)	χ^2 from Fig. 6(a)	χ^2 from Fig. 6(b)
50	2.1 ± 0.4	33 ± 7 (14 ± 4)	0.6	2.5 ± 1.0 (5.9 ± 1.7)	0.05 ± 0.02	5.5 ± 0.9	96 ± 55	0.34 (0.14)	3.1	2.5
150	4.4 ± 0.7	53 ± 10 (33 ± 6)	1.3	3.3 ± 0.7 (5.3 ± 1.1)	0.12 ± 0.04	11.8 ± 2.9	71 ± 45	0.32 (0.20)	2.1	3.1
350	9.3 ± 2.1	75 ± 15 (60 ± 10)	2.2	5.0 ± 1.5 (6.3 ± 1.9)	0.17 ± 0.04	25.9 ± 5.6	66 ± 40	0.10 (0.08)	2.8	2.8

[a]Obtained from the linear fitting in Fig. 6(a).
[b]Calculated from Fig. 2(b) based on Tadday's (Frelin's) data.
[c]Calculated from Fig. 2(a).
[d]Calculated from Eq. (15).
[e]Obtained from the slope of linear fitting in Fig. 6(b) and calculated value of d_h from Fig. 2(a).
[f]Using the range of values of L_a from Frelin's data in Table II only, see text for clarifications.
[g]Calculated from Eq. (13) and the slope of Fig. 6(b) using evaluated values of L_m, L_D, and η_{PS}.

TABLE IV. Comparison of SSA, STA, and TTA of polymers based on literature values.

	Assumed values of					Estimated values of		
Limit	SSA rate κ_{SS} [14] (cm^3/s)	TTA rate κ_{TT} [14] (cm^3/s)	STA rate (κ_{ST}) [14] (cm^3/s)	Singlet lifetime τ_S (s)	Triplet lifetime τ_T (s)	$\tau_S^2 \kappa_{SS}$ (cm^3 s)	$\tau_T^2 \kappa_{TT}$ (cm^3 s)	$\tau_S \tau_T \kappa_{ST}$ (cm^3 s)
Lower	10^{-11}	10^{-14}	10^{-10}	10^{-10}	10^{-5}	10^{-31}	10^{-24}	10^{-25}
Upper	10^{-8}	10^{-11}	10^{-9}	10^{-9}	10^{-3}	10^{-26}	10^{-17}	10^{-21}

with current density is an increasing function of E_k. Using Tadday's values of L_m and L_D, d_h, and $\tau_T^2 \kappa_{TT}$, we find a theoretical increase of 11.7 times in the value of $(\frac{\partial Y_{PS}}{\partial J})_{E_k}$ as E_k increases from 50 to 350 keV. The experimentally obtained increase of $(\frac{\partial Y_{PS}}{\partial J})_{E_k}$ is 3.4 (between 1.9 and 7.0, considering the tolerance limits). However, with a fixed η_{PS} ($\sim 5 \times 10^{-4}$) following the argument abovementioned and Frelin's data on scintillation yield L_m, we find a theoretical increase by a factor 6.8 in the value of $(\frac{\partial Y_{PS}}{\partial J})_{E_k}$ which is within the range of experimental results. Therefore, proceeding forward, we only consider Frelin's data.

Reported fluorescence efficiency values of PS are between 0.1% and 2% at different polymerization ratios due to nonradiative decay that is attributed to the intrinsic rigidity of the large polymer chains [50]. Therefore, our measured fluorescence efficiency of pure PS film η_{PS} agrees well with those reported (0.1%–2%) [50] within experimental errors and under the assumption of isotropic fluorescence emission described in Sec. III for calculating the collection efficiency g. Using the values of $(\frac{\partial Y_{PS}}{\partial J})_{E_k}$, η_{PS}, d_h, L_m, and L_D from Table III (Frelin's data) and Eq. (13), $\tau_T^2 \kappa_{TT}$ is also evaluated in Table III. It can be seen that the evaluated $\tau_T^2 \kappa_{TT}$ is close to the assumed value in the previous section, yielding $J_T \geqslant 1.0 \,\mu\text{A/cm}^2$, i.e., $J_T \approx 5 \times J$ for the maximum value of J. This indicates that the small value approximation in Eq. (8) on the triplet density may result in relatively larger errors at higher current densities used on the experiments than at the lower current densities. As seen in Figs. 2(a) and 4(b) for the high current density $J = 215 \,\text{nA/cm}^2$, the triplet counts between 0 and 10 s are smaller than the counts between 10 and 20 s and the counts at higher integration times are slightly lower, which indicates that the approximation of linearity between triplet saturation density $n_{T\infty}$ and current density J tends to deviate. It can also be seen from Table III that the calculated number of damages created per incident ion L_D from the slope of Fig. 6(b) is one to two orders of magnitude higher than the calculated $E_k L_a$, and $L_D \gg L_m$, considering the values of absolute scintillation yield L_a from Frelin's data. This indicates that on each interaction of the ion with the scintillator molecules, several PS molecules transform into a triplet source. This is indeed not surprising because each dissociated PS molecules form PAHs and radicals that can combine with multiple neighboring molecules [9] and thus may inhibit these neighboring molecules from generating singlet excitons in subsequent irradiation events. The apparent number of damages may also be large because of gradual decrease in the transmitivity of the films with induced dose. We also see that L_D/E_k is higher at lower energies, indicating that low-energy ions create more damage which predicates the reduction of yields. For simplicity, we, however, use a simple

linear fitting as $L_D = S E_k$, yielding a slope $S = L_D/E_k \approx (75 \pm 15)$ defects/keV with a reduced Chi-squared value (χ^2) of 2.2 at $S = 75$ defects/keV.

C. Ionoluminescence emission of doped PS

In Eq. (13) the first term inside the square bracket represents the electrical excitation of primary singlets and the term inside the parentheses that of primary triplets. The triplet-to-singlet up-conversion is linked through $\tau_T^2 \kappa_{TT}$. If a scintillator (fluorophore), having absolute fluorescence efficiency η_{SS}, is added to the film, the fluorophore molecules absorb the singlet emission from the PS matrix via FRET process. The FRET energy transfer efficiency between excited PS singlet state and ground-state fluorophore molecules is given by [51]

$$\eta_{FRET} = \frac{1}{1 + (r/r_0)^6}, \quad (17)$$

where r is the distance an exciton hops between a donor (PS) and the acceptor (fluorophore) molecules and r_0 is the critical distance where the efficiency is 50%. The critical distance r_0, in nanometers, is given by the relation [51]

$$r_0 = 2.108 \times (\kappa_O^2 \eta_{PS} n^{-4} j)^{1/6} \text{ (in nm)}, \quad (18)$$

where j is the spectral overlap integral in M^{-1} cm^{-1} nm^4 and κ_O is called the orientation factor. η_{PS}, as before, is the fluorescence efficiency of pure PS without any acceptor, evaluated in the previous section. The spectral overlap integral j is given by

$$j = \int_0^\infty f_D(\lambda) \varepsilon_A(\lambda) \lambda^4 d\lambda, \quad (19)$$

where $f_D(\lambda)$ is the emission spectra of the donor normalized such that the area under the curve is unity, $\varepsilon_A(\lambda)$ is the absorption spectra of the acceptor scaled to its maximum molar extinction coefficient (ε_{MAX}). Therefore, the fluorescence efficiency of the doped film can be written as

$$\eta_{FL} = \eta_{FRET} \eta_{SS}. \quad (20)$$

To evaluate the FRET efficiency of the doped films η_{FRET}, we take recourse of the measured emission spectra of pure PS film shown in Fig. 3(a), absorption spectra of the fluorophores and their maximum extinction coefficient ε_{MAX} from the PhotoChemCad database [24]. In Fig. 7 the measured emission spectra of undoped PS molecules at three different kinetic energies and the absorption spectra of the four types of fluorophores extracted from Ref. [24] are shown. The PS emission spectra are normalized by the maximum counts at energy $E_k = 350 \,\text{keV}$ in the plot, whereas the absorption spectra of the fluorophores are scaled up to their respective maximum extinction coefficient ε_{MAX}. Since PS medium is
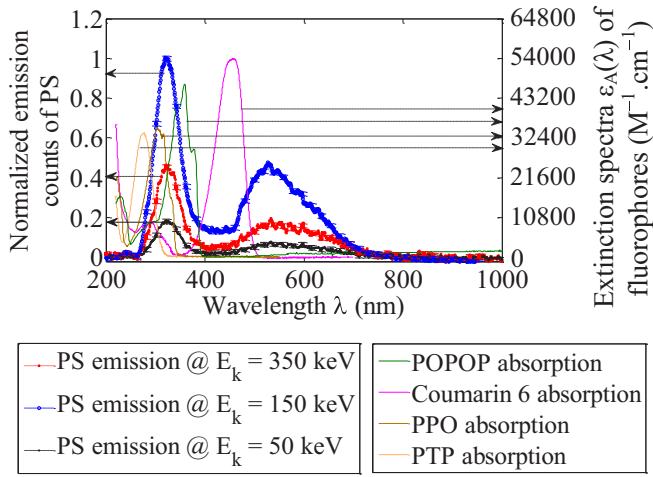
FIG. 7. Measured emission spectra of undoped PS at three different kinetic energies of He$^+$ ions and extracted extinction (absorption) spectra [24] of the four types of fluorophores. The PS emission spectra are normalized by the maximum counts at energy $E_k = 350$ keV. The extracted absorption spectra of the fluorophores are scaled by their respective maximum extinction coefficient ε_{MAX}, listed in Table V.

nonpolar, we assume that the fluorophores do not possess any particular orientation preference in the film and are randomly oriented, which result in a theoretical value of orientation factor $\kappa_O = 2/3$ [51]. We perform the spectral overlap integral from the beginning (1% of the emission maxima) of the singlet band of the PS donors, i.e., 250 nm, and the end of the absorption band of the fluorophore (1% of the extinction maxima). In Table V the reported fluorescence efficiency of the fluorophores η_{SS} calculated spectral overlap integral j and the critical distance r_0 are listed for the four types of fluorophores.

In Figs. 8(a) through 8(d) the measured IL emission spectra of four types of doped PS films are shown. The spectral counts in each case are normalized by the same normalization factor used for undoped PS spectra in Figs. 3(a) and 7. Similar to Fig. 3(a), elimination of the higher order diffraction pattern is performed by subtracting 24% of the counts between $200 \leqslant \lambda \leqslant 500$ nm from the counts between $400 \leqslant \lambda \leqslant 1000$ nm. It can be seen that only about 4% of the primary peaks are still observable in the corrected spectra, indicating that the higher order diffraction pattern correction indeed eliminates a significant amount of artifact from the entire emission spectra. Also, since these artifact bands are clearly separated from the singlet band of the fluorophores' emission spectra, they have no effect on the following calculations of singlet yield as only the singlet band is considered for the photon counts.

POPOP and Coumarin 6 show significant emission above 400 and 450 nm, respectively. The small peaks close to 320 nm in the POPOP and Coumarin 6 spectra correspond to singlet emission from PS itself. Since the PS emission spectra in the doped film can be identified separately for POPOP and Coumarin 6 samples, FRET efficiency η_{FRET} can be directly evaluated by comparing the intensity of the PS spectra in the doped film and the undoped film as [51]

$$\eta_{\text{FRTET}} = \left(1 - \frac{F_d}{F_u}\right), \qquad (21)$$

TABLE V. Semiempirical calculation of η_{FRET}, spectral overlap integral j, and fluorescence efficiency η_{FL}.

Fluorophore	η_{SS}^a	ε_{MAX}^a (M^{-1} cm^{-1})	$10^{-13} \times j$ (M^{-1} cm^{-1} nm^4)	r_0^b (nm)	E_k (keV)	$1:m$	η_{FRET}	r (nm)	η_{FL}	Mean η_{FL}
POPOP	0.93	47 000	30.9	1.08	350	1/300	0.75 ± 0.01	0.90 ± 0.01	0.70 ± 0.01	0.79 ± 0.10
					150		0.91 ± 0.02	0.73 ± 0.02	0.85 ± 0.02	
					50		0.92 ± 0.03	0.72 ± 0.03	0.86 ± 0.03	
					350	1/3000	0.68 ± 0.01	0.95 ± 0.01	0.67 ± 0.01	0.70 ± 0.05
					150		0.68 ± 0.02	0.95 ± 0.02	0.67 ± 0.02	
					50		0.72 ± 0.03	0.92 ± 0.03	0.71 ± 0.03	
Coumarin 6	0.78	54 000	16.0	0.97	350	1/30	0.72 ± 0.01	0.83 ± 0.01	0.56 ± 0.01	0.63 ± 0.07
					150		0.73 ± 0.02	0.82 ± 0.02	0.57 ± 0.02	
					50		0.83 ± 0.04	0.74 ± 0.04	0.66 ± 0.04	
					350	1/300	0.52 ± 0.01	0.96 ± 0.01	0.40 ± 0.01	0.45 ± 0.06
					150		0.63 ± 0.02	0.87 ± 0.02	0.49 ± 0.02	
					50		0.53 ± 0.04	0.95 ± 0.03	0.41 ± 0.03	
PPO	1.00	35 700	16.8	0.97	–	–	–	–	–	–
PTP	0.93	33 800	3.6	0.75	–	–	–	–	–	–

^{a}From Ref. [24].
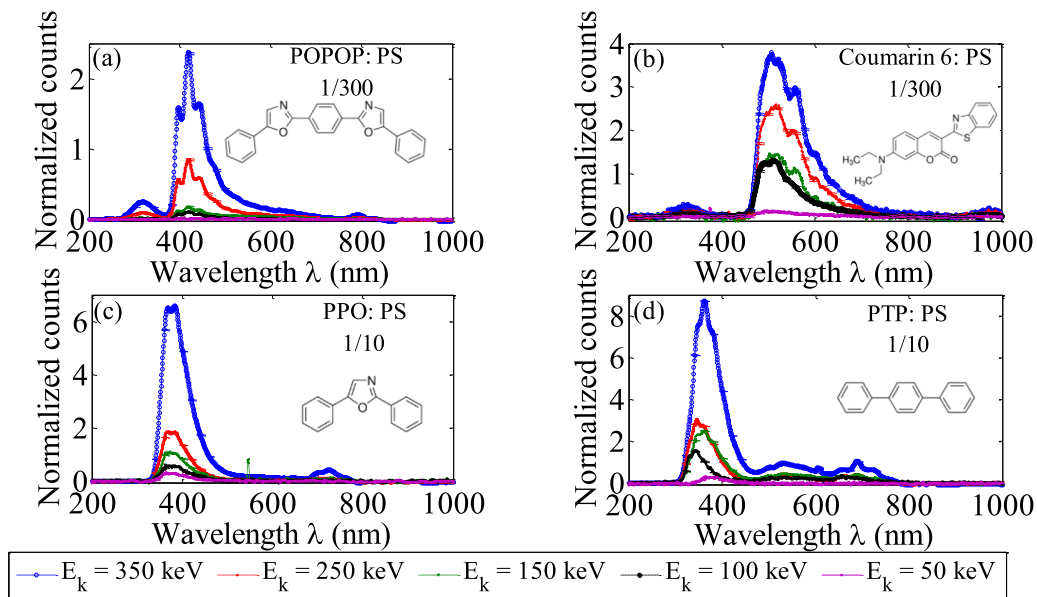^{b}Calculated standard deviation less than 10 pm in all cases.

FIG. 8. IL spectra from doped PS films with (a) POPOP, (b) Coumarin 6, (c) PPO, and (d) PTP as secondary scintillators at some specific mass ratios (displayed in the corresponding figures). $J = (200 \pm 5)$ nA. $E_k = 350$ keV. The counts are normalized by the same factor used for normalization of pure PS singlet emission results shown in Fig. 3.

where F_d and F_u are the intenities of PS emission in the doped and undoped films, respectively, obtained by integrating the counts over the emission spectra of PS ($250 \leqslant \lambda \leqslant 400$ nm). In Table V these mesured FRET efficiciencies are listed for POPOP and Coumarin 6 samples at three kinetic energies and two different mass ratios 1:m used in our experiments. With the calculated values of r_0 and the measured values of η_{FRET}, the distance r is also estimated and listed in Table V. For PPO and PTP, the PS emission spectra cannot be distinguished from the fluorophore's emission spectra and hence, measurement of FRET efficiency and calculation of r have been avoided.

It can be seen that within the doping ranges used in the experiments, the FRET efficiencies are above 50% for POPOP and Coumarin 6 samples and hence the distance r is smaller than the calculated critical distance r_0. These semiempirical values of r decrease as the concentration of the fluorophore in the PS matrix increases, indicating that with increased fluophore concentration, the excitons hop lesser distance before being captured by the fluorophore [52]. In the last two columns of Table V, the fluoresecence efficiency of the doped films is calculated based on Eq. (20). It can be seen that the fluorescence efficiency is higher at higher dopant concentration due to different energy transfer efficiencies. The emission yield is also expected to depend on the number of fluorophore molecules available to capture the excitons generated from the primary scintillator sites. There can also be concentration dependent self-quenching of the fluorescence yield at high mass ratios of the fluorophore (above 1%–2%) [7,23,53–57]. Formation of ground-state aggregation among the fluorophore molecules is a common mechanism for such quenching [55]. There is also a possibility of dynamic quenching via interactions between PS and fluorophore molecules [7,53,54,57]. In both cases, the fluorescence emission intensity decreases with increasing fluorophore concentrations, either by reducing the available number of fluorophores (static

quenching) or by introducing concentration-dependent nonradiative decay pathways (dynamic quenching). Zaushitsyn *et al.* [58] showed that the singlet-triplet annihilation mechanism can lead to quenching as $(1/m)^{-1/2}$. At very large excitation densities, SSA of fluorophore molecules also can contribute to a $(1/m)^{-1/2}$ dependence of the fluorescence efficiency [23]. The overall effect of fluorophore concentration on the yield of the doped films is therefore nontrivial. This additional mass dependence of the overall yield, apart from the observed mass dependence of the fluorescence efficiency η_{FL}, can be incorporated by using an arbitrary unitless factor K_M which is a function of mass ratio. We expect this value to be lower than, or at best, of the order of, the mass ratio $1/m$.

The addition of the fluorophores may have two other effects on the emission properties:

(1) The triplet to singlet up-conversion factor $\tau_T^2 \kappa_{TT}$ may change in the doped samples. Several authors demonstrated that triplet-triplet annihilation takes place via Dexter process between a pair of excited triplet states [52,59,60]. Several authors have demonstrated that with increasing doping, TTA rate [13,52,61] and TTA-mediated singlet up-conversion [62] increase. In [62], Singh-Rachford and Castellano showed that singlet up-conversion enhances by several factors by introducing the dopant, before the enhancement saturates beyond certain dopant concentration. Zhang *et al.* [52] have shown by measurement and curve fitting that an increase of dopant concentration by a factor of 8 increases the TTA rate κ_{TT} by 2–4 times and decreases the triplet lifetime τ_T by 20%–60% depending on the dopant type in a 4,4′-N,N′-dicarbazole-biphenyl hosted sample. Calculations based on their reported results [52] show an increase of 2–14 times in the value of the product $\tau_T^2 \kappa_{TT}$ as the concentration of different types of dopants incrases by the factor 8. Baldo *et al.* [13] have shown that within very similar inital triplet densities and sample types, κ_{TT} increases by a factor 2 and τ_T reduces by
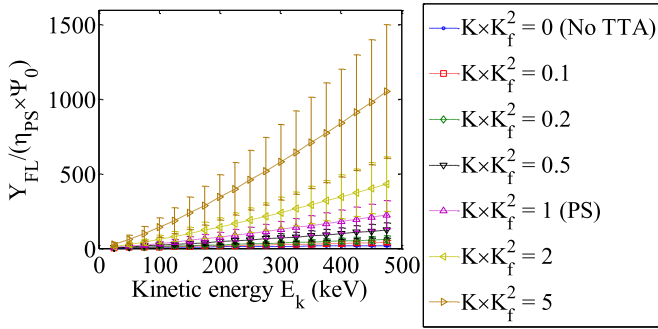
FIG. 9. Simulated singlet yield using Eq. (25), normalized by the factor $\eta_{PS}\Psi_0$ for different values of KK_f^2 at $J = 200\,\text{nA/cm}^2$. $KK_f^2 = 1$ represents pure PS film. $KK_f^2 = 0$ represents no TTA. For the simulations, Frelin's data of L_m are used. The error bars are calculated based upon the longitudinal straggle on projected range d_h [shown in Fig. 2(a)], ± 15 defects/keV tolerance on evaluated damages per ion for PS films L_D and the upper and lower range of values of L_m based on Frelin's data (see Table II).

nearly 25% as dopant concentrations are increased by a factor 20, leading to an increase of 1.4 in the product $\tau_T^2\kappa_{TT}$. We multiply a factor K to the $\tau_T^2\kappa_{TT}$ of pure PS samples to account for this change in the doped sample, such that $K = 1$ indicates pure PS sample.

(2) Doping of the fluorophores could change the radiation hardness of the films depending on the type and amount of the molecular groups in the PS chains. This would lead to different singlet quenching half-life t_f. For PTP doped PVT, Quanta [4] showed a reduction by a factor of 3 in the t_f value under He$^+$ ion irradiation. Senchishin *et al.* [63] performed a detailed investigation of the effect of several types of doping on PS. They showed that addition of a metalorganic stabilizer and a diffusion enhancer increases the radiation hardness of

the otherwise low radiation-hardness PS-based scintillators. We accommodate this possible change of radiation hardness of our samples by multiplying another factor K_f to the damage created per ion incidence L_D such that $K_f = 1$ indicates pure PS sample. After measuring t_f from the doped samples, K_f can be evaluated by comparing with pure PS at the same E_k and J.

The singlet yield of the doped film can be therefore written by analogy with Eq. (13) as

$$Y_{FL}(E_k, J)$$
$$= \eta_{FL}K_M\left[\frac{1}{4}L_m + \frac{1}{8}K\frac{\tau_T^2\kappa_{TT}}{qd_h}\left(\frac{3}{4}L_m + K_fL_D\right)^2 J\right]. \quad (22)$$

Therefore, two enhancement parameters can be defined between the singlet yield of undoped and doped scintillator, as

$$\Psi_0 = \frac{Y_{FL}(E_k, 0)}{Y_{PS}(E_k, 0)} = \left(\frac{\eta_{FL}}{\eta_{PS}}\right)K_M \quad (23)$$

and

$$\Psi_S = \frac{\left(\frac{\partial Y_{FL}}{\partial J}\right)_{E_k}}{\left(\frac{\partial Y_{PS}}{\partial J}\right)_{E_k}} \approx \Psi_0KK_f^2 \quad (24)$$

as $L_D \gg L_m$. This simplifies Eq. (22) as

$$Y_{FL}(E_k, J) \approx \eta_{PS}\left[\frac{1}{4}\Psi_0L_m + \frac{1}{8}\Psi_S\frac{\tau_T^2\kappa_{TT}}{qd_h}L_D^2 J\right]. \quad (25)$$

The advantage of defining these two parameters is that Ψ_0 and Ψ_S can be experimentally evaluated from yield vs current density plot, or yield vs kinetic energy plot of the fluorophores from the known values of L_m, $\tau_T^2\kappa_{TT}$, L_D, and η_{PS} already evaluated for pure PS, and then by comparing with those of undoped PS films. Once these two are known, KK_f^2 can be evaluated from Eq. (24) and K_M can be evaluated from Eq. (23) for POPOP and Coumarin 6 only. On the other hand, the
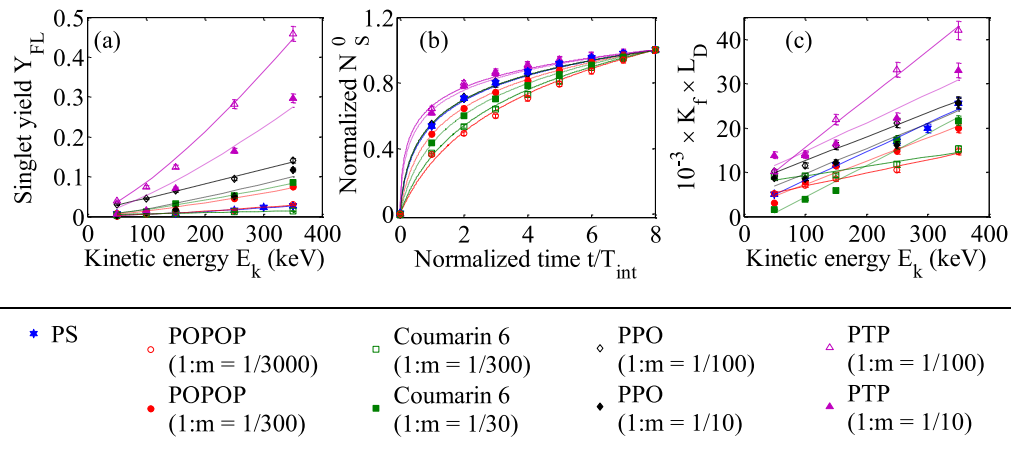

FIG. 10. (a) Evaluation of singlet yield as a function of energy of He$^+$ ions from measured time evolution of photon emission from the doped films. The evaluated yield is fitted to Eq. (26) to extract best-fit values of yield enhancement factors Ψ_0 and Ψ_S. The fitted results are shown as dashed lines in the same color as the data markers. (b) Evolution of singlet emission per unit area $N_S^O(t)$ with irradiation time for undoped PS and different doped scintillators listed in Table II. Current density $J = (200 \pm 5)\,\text{nA/cm}^2$, energy, $E_k = 350\,\text{keV}$. Each plot is normalized by their respective maxima attained after eight integration periods. For each case, integration time of the spectrometer is $T_{int} = 10\,\text{s}$. Yield Y_{FL} in (a) is evaluated by logarithmic fitting of (b) using Eq. (12) and finding the slope at $t = 0$. (c) Evaluated damage creation per incident ion from the measured singlet quenching half-life t_f as a function of incident energy. t_f, is first evaluated from the fitting of (b) and then Eq. (2a) is used to find K_fL_D where L_D is replaced with K_fL_D for the doped films.

TABLE VI. Calculated yield enhancement for doped scintillators with He$^+$ ($J = 200\,\text{nA/cm}^2$).

Fluorophore	1:m	Ψ_0[a]	Ψ_S[a]	K	K_f	K_M[b]	χ^2 from Fig. 10(a)	χ^2 from Fig. 10(c)
None[a]	–	1.0	1.0	1.00	1.00	1.0	0.91	2.16
POPOP	1/3000	0.7 ± 0.3	0.5 ± 0.3	2.86	0.50	5.0×10^{-4}	1.71	2.81
	1/300	1.7 ± 0.3	3.7 ± 1.4	4.08	0.73	10.8×10^{-4}	1.08	1.51
Coumarin 6	1/300	0.7 ± 0.2	2.4 ± 1.1	8.64	0.63	7.8×10^{-4}	2.31	3.10
	1/30	1.8 ± 0.3	1.3 ± 0.2	0.85	0.92	14.3×10^{-4}	1.23	2.53
PPO	1/100	2.0 ± 0.3	7.4 ± 1.3	4.57	0.90	–	3.06	2.23
	1/10	2.1 ± 0.3	7.8 ± 0.9	4.69	0.89	–	1.71	2.61
PTP	1/100	4.1 ± 0.2	20.1 ± 2.7	2.57	1.38	–	2.18	2.21
	1/10	3.4 ± 0.2	13.9 ± 1.8	2.75	1.22	–	2.85	3.16

[a]Pure PS: Ψ_0, Ψ_S, K_f, and K are unity as reference by definition, both in calculation and in measurements.
[b]Calculated using Eq. (23) and values of η_{FL} listed in Table V.

change of damage creation due to doping K_f can be separately evaluated by experimentally finding the singlet quenching half-life t_f and then comparing the number of damages created per ion in the doped films with that in undoped PS. Finally, the TTA multiplication factor K can be evaluated from the known values of Ψ_0, Ψ_S, and K_f.

In Fig. 9 some calculated values of $\left(\frac{Y_{FL}}{\eta_{PS}\Psi_0}\right)$ are plotted using Eq. (25) for different values of $\Psi_S/\Psi_0 = K K_f^2$ between 0 and 10 and $J = 200\,\text{nA/cm}^2$ assuming $L_D \gg L_m$ and L_m calculated based on Frelin's data (Table II). We used an evaluated average value $\tau_T^2 \kappa_{TT} = 0.25 \times 10^{-21}\,\text{cm}^3\,\text{s}$ from Table III and $L_D/E_k = 75$ defects/keV already evaluated for PS. In Fig. 9 $K K_f^2 = 0$ indicates no TTA and $K K_f^2 = 1$ is for pure PS film. For low $K K_f^2$ values ($K K_f^2 \ll 1$), Y_{FL} is close to $\frac{1}{4}\eta_{FL}L_m$ and a nonlinearity between Y_{FL} and L_m is seen for higher values of $K K_f^2$ for which L_D^2 dominates the yield. The error bars are calculated by considering the longitudinal straggle on the projected range d_h [shown in Fig. 2(a)], ±15 defects/keV tolerance on evaluated damages per ion for PS films L_D, and the upper and lower range of values of L_m based on Frelin's data (see Table II). The large error bars represent a significant uncertainty in the estimated values of yield, ranging between 41% and 45% of the plotted mean values in the range 50–350 keV.

In Fig. 10(a) the measured singlet yield of the eight doped films Y_{FL} are plotted agains the applied kinetic energy E_k of He$^+$ ions. Current density in each case is $J = (200 \pm 5)\,\text{nA/cm}^2$. Similar to Fig. 4(b), first, the photons

counts from the spectrometer are recorded over several integration periods and the time dependent emission per unit area is fitted to the logarithmic fitting equation (12). The time evolution of the emission counts per unit area N_S^O is shown in Fig. 10(b) which is normalized by the respective maxima attained after eight integration periods of the spectrometer. Y_{FL} is calculated from the slope of Fig. 10(b) at time $t = 0$. Finally, Y_{FL} is fitted to Eq. (25) to find the best-fit results of the yield enhancement factors Ψ_0 and Ψ_S. These best-fit results are furnished in Table VI. The fitting results in a reduced Chi-squared error (χ^2) between 0.91 and 3.06 between the different films. It can be noted that the large uncertainty of up to 45% in the simulated value of yield for a given value of K and K_f^2 are not considered in the χ^2 results. If, as an altrnative, we consider the root mean squared standard deviation of the simulated yield from Fig. 9 and that of the measured yield, the χ^2 values reduce to the range 0.11 and 0.81, indicating that all the measured yield values are well withing the range of posssible yield values for a given fitted value of K and K_f. Yield variation with current density J similar to Fig. 6(a) for pure PS is performed later, in Fig. 11(a).

Similar to the case of pure PS film [Fig. 4(b)], the effect of irradiation induced damage on the emission from the doped PS films can also be well described with the singlet quenching factor $Q_S(t)$. From the logarithmic fitting in Fig. 10(b), the singlet quenching half-lives t_f are also evaluated using Eq. (2a). The Chi-squared error (χ^2) of the logarithmic fitting in Fig. 10(b) are between 0.46 and 0.92 for all the doped samples, indicating a good fit. In Fig. 10(c) the evaluated damage created
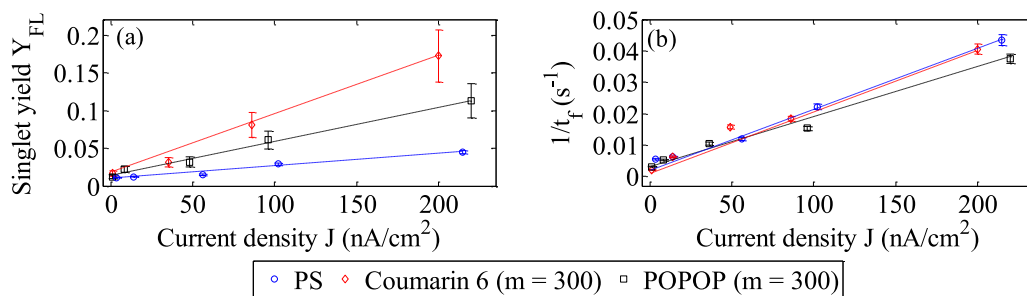

FIG. 11. (a) Evaluated singlet yield $Y_{FL}(E_k, J)$ and (b) t_f^{-1} of POPOP and Coumarin 6 films with mass ratio $1 : m = 1/300$ in both cases from their measured emission spectra and its time evolution. Kinetic energy $E_k = 350\,\text{keV}$. The straight lines in the same color as the data markers are the linearly fitted results.

TABLE VII. Comparison of yield enhancement from Y_{FL} vs E_k and Y_{FL} vs J.

| Scintillator | 1:m | Ψ_0 from | | Ψ_S from | | K_f from | | χ^2 from Fig. 11(a) | χ^2 from Fig. 11(b) |
		Y_{FL} vs E_k	Y_{FL} vs J	Y_{FL} vs E_k	Y_{FL} vs J	$K_f L_D$ vs E_k.	t_f^{-1} vs J		
POPOP	1/300	1.7 ± 0.3	1.5 ± 0.3	3.7 ± 0.8	4.3 ± 0.6	0.73	1.07 ± 0.11	1.06	2.51
Coumarin 6	1/300	0.7 ± 0.2	1.0 ± 0.2	2.4 ± 0.4	3.1 ± 0.4	0.63	0.75 ± 0.08	0.68	2.26

per incident ion $K_f L_D$ of the eight doped films are shown. $K_f L_D$ is evaluated by first finding a singlet quenching half-life t_f from Fig. 10(b) and then using Eq. (2a), where L_D is replaced by $K_f L_D$ for the doped films. Since $L_D/E_k = (75 \pm 15)$ defects/keV for pure PS [also shown on the same plot, Fig. 10(c)], a linear fit is used between $K_f L_D$ and energy E_k and from the slope K_f are evaluated. Evaluation of $K_f L_D$ is repeted by varying the beam current density J later in Fig. 11(b) similar to Fig. 6(b) for pure PS. The linear fit produces a reduced Chi-squared error (χ^2) between 1.51 and 3.31 for all the samples, indicating a poor fit. However, it can be noted that the linearity between the damages created and energy of the incident ion ($L_D/E_k = 75$) is only a simplified assumption for ease of calculations and may not reflect the damage creation mechanism accurately. If the large (20%) uncertainty in the value of L_D/E_k is incorporated, similar to the calculations of yield Y_{FL}, discussed in the previous paragraph, the modified χ^2 values range between 0.84 and 1.31.

From the best-fit results of Ψ_0 and Ψ_S in Table VI, the values of the multiplication parameters K, K_f, and K_M are evaluated in Table VI. It can be seen from Table VI that for low doping concentrations of POPOP ($1:m = 1/3000$ and $1/300$) and Coumarin 6 ($1:m = 1/300$), damage increase factor K_f is considerably lower than unity, indicating a less amount of PAHs created than in pure PS. POPOP is known as a nonradiation hard secondary scintillator in commonly used recipe of PS-based scintillators (PS + 2% PTP + various % of POPOP) [63] where increasing POPOP concentration to more than 0.02% leads to reduced hardness. The increase of damage creation K_f with increasing concenration of POPOP ($1:m = 1/3000$ and $1:m = 1/300$ in Table IV correspond to 0.03% and 0.3% POPOP, respectively) and Coumarin 6 resembles this phenomenon. For PPO, K_f is close to unity, indicating that the functionalizing of the PS chains with the oxazole group of PPO does not change its radiation hardness significantly; however, considerable increase in tripplet to singlet up-conversion is attained through increased K. For PTP, K_f is larger than that for all other fluorophores, indicating low radiation hardness and increased PAH formation. Larger than unity values of both K_f and K for PTP lead to higher singlet yield as shown in Table VI.

Considerable yield enhancement is achieved using the doped scintillators due to the increase in both fluorescence efficiency and triplet-to-singlet up-conversion as reflected by the values of K and K_f. However, the values of K_M are considerably lower than unity owing to low doping ($1/m \ll 1$) and possible self-quenching.

The values of K, the factor determining enhancement of TTA induced singlet states, are higher than unity for the doped samples except Coumarin 6 ($1:m = 1/30$). For POPOP, an increase of doping by 10 times increased the $\tau_T^2 \kappa_{TT}$ value by a

factor 1.4, agreeing well with the results reported in [13,52]. For PPO and PTP samples, the values increase only by 2% and 7%, respectively, indicating saturation of the enhancement effect at such high concentrations as shown by Singh-Rachford and Castellano [62], whereas for Coumarin 6, the evaluated K significantly reduces as the concentration is increased. These results show that the TTA mediated singlet up-conversion is strongly dependent on the concentration and type of the dopant, and warrants further investigation.

To confirm the effect of TTA, we also performed yield measurements from POPOP and Coumarin 6 doped samples by varying the current density J keeping E_k constant. In Figs. 11(a) and 11(b) the singlet yield Y_{FL} and the quenching half-life t_f are measured for POPOP ($1 : m = 1/300$) and Coumarin 6 ($1 : m = 1/300$) as a function of He$^+$ ion current density at $E_k = 350$ keV. For comparison, we also plotted the values for pure PS film. By linear fitting of Y_{FL} with J, $Y_{FL}(E_k, 0)$, and $(\frac{\partial Y_{FL}}{\partial J})_{E_k}$ are evaluated to find the yield enhancement factors Ψ_0 and Ψ_S. Similarly, by linear fitting the inverse of singler quenching half-life, i.e., t_f^{-1}, with J, K_f values are evaluated and compared with those obtained in Table IV. The results ar furnished in Table VII.

It is seen by comparing the values of Ψ_0, Ψ_S, and K_f from Tables IV and V that both the processes produce similar values of yield enhancement within the experimental errors. Thus, the model Eq. (22) satisfactorily describes the behaviors of singlet emission yields in the doped films.

VI. CONCLUSIONS

In this article we have developed an understanding of the IL properties of undoped and doped scintilator films in low kineic energy ranges, through a theoretical model by incorporating semiempirical scintillation generation formula, irradiation induced damage, and the photophysical energy transfer mechanisms in the evolution of triplet and singlet excited states of the scintillators. Our work has shown that for the pure, undoped PS films the triplet exciton density remains nearly constant over the entire irradiation duration, and the triplet exciton density is nearly proportional to the ion current density. In our model, we have incorporated the effect of triplet-triplet annihilation mechanism and shown that the triplet exciton density significantly contributes to the singlet emission yield of the undoped and doped scintillators. We have also shown that for the doped films, the enhanced fluorescence efficiency, energy transfer efficiency from the PS matrix to the fluorophores, and enhnced triplet to singlet up-conversion result in increased scintillation yield. Such understanding can provide deeper insight into the scintillation and ionouminescnce properties of organic scintillators.

[1] L. L. W. Wang, L. A. Perles, L. Archambault, N. Sahoo, D. Mirkovic, and S. Beddar, Phys. Med. Biol. **57**, 7767 (2012).

[2] S. Kim, S. B. Lee, S. H. Yoo, S. Cho, D. W. Kim, D. Shin, S. Y. Park, C. H. Kim, and S. H. Lee, Jpn. J. Appl. Phys. **51**, 046401 (2012).

[3] A. S. Beddar, T. M. Briere, F. A. Mourtada, and O. N. Vassiliev, Med. Phys. **32**, 1265 (2005).

[4] A. Quaranta, Nucl. Instrum. Methods Phys. Res. B **240**, 117 (2005).

[5] V. I. Tretyak, Astropart. Phys. **33**, 40 (2010).

[6] D. Broggio, J. M. Jung, R. Barillon, and T. Yamauchi, Rad. Meas. **40**, 736 (2005).

[7] H. Nakamura, H. Kitamura, O. Shinji, K. Saito, Y. Shirakawa, and S. Takahashi, Appl. Phys. Lett. **101**, 261110 (2012).

[8] H. M. Lee, Y. N. Kim, B. H. Kim, S. O. Kim, and S. O. Cho, Adv. Mater. **20**, 2094 (2008).

[9] E. Kim, J. Kyhm, J. H. Kim, G. Y. Lee, D.-H. Ko, I. K. Han, and H. Ko, Sci. Rep. **3**, 3253 (2013).

[10] D.-M. Mei, Z.-B. Yin, L.C. Stonehill, and A. Hime, Astropart. Phys. **30**, 12 (2008).

[11] L. Reichhart *et al.*, Phys. Rev. C **85**, 065801 (2012).

[12] K. W. Jang, W. J. Yoo, J. K. Seo, J. Y. Heo, J. Moon, J.-Y. Park, E. J. Hwang, D. Shin, S.-Y. Park, H.-S. Cho, and B. Lee, Nucl. Instrum. Methods Phys. Res. A **652**, 841 (2011).

[13] M. A. Baldo, C. Adachi, and S. R. Forrest, Phys. Rev. B **62**, 10967 (2000).

[14] C. Gartner, C. Karnutsch, U. Lemmer, and C. Pflumm, J. Appl. Phys. **101**, 023107 (2007).

[15] A. F. Adadurov, P. N. Zhmurin, V. N. Lebedev, and V. V. Kovalenko, Nucl. Instrum. Methods Phys. Res. A **621**, 354 (2010).

[16] J. Boivin, S. Beddar, M. Guillemette, and L. Beaulieu, Med. Phys. **42**, 6211 (2015).

[17] J. Boivin, S. Beddar, C. Bonde, D. Schmidt, W. Culberson, M. Guillemette, and L. Beaulieu, Phys. Med. Biol. **61**, 5569 (2016).

[18] D. E. Hyer, R. F. Fisher, and D. E. Hintenlang, Med Phys. **36**, 1711 (2009).

[19] A.-M. Frelin, J.-M. Fontbonne, G. Ban, J. Colin, and M. Labalme, IEEE Trans. Nucl. Sci. **55**, 2749 (2008).

[20] F. Lessard, L. Archambault, M. Plamondon, P. Després, F. T. Proulx, S. Beddar, and L. Beaulieu, Med. Phys. **39**, 5308 (2012).

[21] A. Mapelli, PhD. Dissertation, Thesis no. 5033, École polytechnique Fédérale de Lausanne, Switzerland, 2011.

[22] P. Finocchiaro, Proc. 15th Int. Conf. Appl. Acc. Res. Ind, Denton, USA (1998).

[23] S. Chakraborty, K. Harris, and M. Huang, AIP Adv. **6**, 125113 (2016).

[24] http://www.photochemcad.com/pages/chemcad/chem-home.html.

[25] http://www.chemspider.com/Search.aspx.

[26] https://oceanoptics.com/product/qe-pro/.

[27] http://www.spectralproducts.com/pdf/s7031-1006.pdf.

[28] Email communication with technical specialist at OceanOptics.

[29] See Supplemental Material at http://link.aps.org/supplemental/10.1103/PhysRevMaterials.1.055201 for 1. Calibration of the OceanOptics spectrometer and 2. Ion-beam current density variation and its effect on the steady-state ionoluminescence measurement.

[30] ftp://download.newport.com/Photonics/Power%20Meters/Obsolete%20Products/1916-C%20and%20-R/1916-C_R_Manual_Rev_G.pdf

[31] J. Hong, W. W. Craig, P. Graham, C. J. Hailey, N. J. C. Spooner, and D. R. Tovey, Astropart. Phys. **16**, 333 (2002).

[32] C. Aberle, C. Buck, F.X. Hartmann, S. Schonert, and S. Wagner, J. Instrum. **6**, P11006 (2011).

[33] A. Tadday, Ph.D. Dissertation, Ruperto-Carola-University of Heidelberg, Germany, 2011.

[34] L. Torrisi, Nucl. Instrum. Methods Phys. Res. B **170**, 523 (2000).

[35] Saint Gobain Plastic scintillator brochure: http://www.crystals.saint-gobain.com/sites/imdf.crystals.com/files/documents/organics-brochure.pdf.

[36] J. F. Williamson, J. F. Dempsey, A. S. Kirov, J. I. Monroe, W. R. Binns, and H. Hedtjarn, Phys. Med. Biol. **44**, 857 (1999).

[37] M. N. Peron and P. Cassette, Nucl. Instrum. Methods Phys. Res. A **369**, 344 (1996).

[38] T. Doke, A. Hitachi, J. Kikuchi, K. Masuda, H. Okada, and E. Shibamura, Jpn. J. Appl. Phys. **41**, 1538 (2002).

[39] R. L. Craun and D. L. Smith, Nucl. Instrum. Methods **80**, 239 (I970).

[40] http://www.srim.org/SRIM/SRIMLEGL.htm.

[41] J. L. Magee and J.-T. J. Huang, J. Phys. Chem. **76**, 3801 (1972).

[42] N. Markovic, Z. Siketic, D. Cosic, H. K. Jung, N.H. Lee, W.-T. Han, and M. Jakšic, Nucl. Instrum. Methods Phys. Res. B **343**, 167 (2015).

[43] C. Manfredotti, S. Calusi, A. Lo Giudice, L. Giuntini, M. Massi, P. Olivero, and A. Re., Diam. Relat. Mater. **19**, 854 (2010).

[44] J. M. Torkelson, S. Lipsky, M. Tirrell, and D. A. Tirrell, Macromolecules **16**, 326 (1983).

[45] G. A. George, J. Appl. Poly. Sci. **18**, 117 (1974).

[46] https://www.mathworks.com/products/curvefitting.html.

[47] P. A. Lane, L. C. Palilis, D. F. O'Brien, C. Giebeler, A. J. Cadby, D. G. Lidzey, A. J. Campbell, W. Blau, and D. D. C. Bradley, Phys. Rev. B **63**, 235206 (2001).

[48] D.H.S. Yu and J. M. Torkelso, Macromolecules **21**, 852 (1988).

[49] D. J. Rey, B. Zurro, G. García, A. Baciero, L. R. Barquero, and M. G. Munoz, J. Appl. Phys. **104**, 064911 (2008).

[50] M. A. Winnik, *Photophysical and Photochemical Tools in Polymer Science: Conformation, Dynamics, Morphology*, Springer Science & Business Media (Springer, Berlin, 2012), p. 441.

[51] *IUPAC. Compendium of Chemical Terminology*, 2nd ed. (the "Gold Book"). Compiled by A. D. McNaught and A. Wilkinson (Blackwell Scientific, Oxford, 1997).

[52] Y. Zhang and S. R. Forrest, Chem. Phys. Lett. **590**, 106 (2013).

[53] H. Nakamura, Y. Shirakawa, H. Kitamura, N. Sato, O. Shinji, K. Saito, and S. Takahashi, Sci. Rep. **3**, 2502 (2013).

[54] D. N. McKinsey, C. R. Brome, J. S. Butterworth, R. Golub, K. Habicht, P. R. Huffman, S. K. Lamoreaux, C. E. H. Mattoni, and J. M. Doyle, Nucl. Instrum. Methods Phys. Res. B **132**, 351 (1997).

[55] S. Hamann, J. F. Kiilgaard, T. Litman, F. J. A. Leefmans, B. R. Winther, and T. Zeuthen, J. Fluor. **12**, 139 (2002).

[56] A. Andersson, J. Danielsson, A. Gräslund, and L. Mäler, Eur. Biophys. J. **36**, 621 (2007).

[57] C. W. Tang, S. A. VanSlyke, and C. H. Chen, J. Appl. Phys. **65**, 3610 (1989).

[58] Y. Zaushitsyn, K. G. Jespersen, L. Valkunas, V. Sundström, and A. Yartsev, Phys. Rev. B **75**, 195201 (2007).

[59] J. C. Ribierre, A. Ruseckas, K. Knights, S. V. Staton, N. Cumpstey, P. L. Burn, and I. D. W. Samuel, Phys. Rev. Lett. **100**, 017402 (2008).

[60] E.B. Namdas, A. Ruseckas, and I. D. W. Samuel, Appl. Phys. Lett. **86**, 091104 (2005).

[61] Q. Wang and H. Aziz, Appl. Phys. Lett. **105**, 053304 (2014).

[62] T. N. Singh-Rachford and F. N. Castellano, Coord. Chem. Rev. **254**, 2560 (2010).

[63] V. G. Senchishin, F. Markley, V. N. Lebedev, V. E. Kovtun, V. S. Koba, A. V. Kuznicbenko, V. D. Tizkaja, J. A. Budagov, G. Bellettini, V. P. Sehnozbenko, I. I. Zalubovsky, and I. E. C.-Zorin, Nucl. Instrum. Methods Phys. Res. A **364**, 253 (1995).